THREE-DIMENSIONAL COMPRESSIBLE STABILITY-TRANSITION CALCULATIONS USING THE SPATIAL THEORY

by
R. Niethammer* and D. Arnal**
ONERA/CERT, Toulouse, France
and
V. de Laharpe†, H. H. Chen†† and T. Cebeci†††
California State University, Long Beach

Abstract

The e^n-method is employed with the spatial amplification theory to compute the onset of transition on a swept wing tested in transonic cryogenic flow conditions. Two separate eigenvalue formulations are used. One uses the saddle-point method and the other assumes that the amplification vector is normal to the leading edge. Comparisons of calculated results with experimental data show that both formulations give similar results and indicate that the wall temperature has a rather strong effect on the value of the n factor.

1. Introduction

In the absence of leading-edge contamination and Görtler instability, it is well known that transition on swept wings may occur either due to streamwise instability (related to the properties of the streamwise velocity profile u) or cross-flow instability (related to the properties of the cross-flow velocity profile w). Since the u-profiles look like Falkner-Skan profiles, the streamwise instability is similar to that of a two-dimensional flow and leads to turbulence in flows with positive pressure gradient. On the other hand, the development of a cross-flow profile is characterized by an inflectional instability that can induce transition in flows with a negative pressure gradient.

In order to design new aircraft wings, one must be able to predict transition on swept wings. The most popular method for predicting transition is the e^n-method, which was initially developed for two-dimensional flows[1,2]. This method is based on the solution of the Orr-Sommerfeld equation using either temporal or spatial amplification theory. In either approach the integrated amplification rates A/A_0 of the unstable frequencies are determined, and transition is computed on the assumption that it occurs when the ratio A/A_0 of the locally most unstable wave reaches a critical value e^n, with n between 8 and 10 for a low disturbance environment.

In the extension of this method to three-dimensional flows, both temporal and spatial amplification theories can again be used. In the former case, the eigenvalue problem involves five scalars α, β, ω_r, ω_i and R and in the latter case it involves six scalars α_r, α_i, β_r, β_i, ω and R. In both approaches, the solution procedure is considerably more difficult than its counterpart in two-dimensional flows because the nontrivial solution of the linear stability equations in three-dimensional flows provides only two relations

between the eigenvalues α, β, ω and R. To predict transition for example, in spatial amplification theory, ω and R are prescribed, so two new relations between α and β are required before the solution of the linear stability equations can be obtained.

To date, most problems of the three-dimensional transition problems employing linear stability theory have been treated by using the temporal theory. When R and ω_r are specified, the values of α and ω_i are not unique, since they both are functions of β [$\alpha = \alpha(\beta)$ and $\omega_i = \omega_i(\beta)$]. A possible solution is to determine the wave number direction $\psi = \tan^{-1}(\beta/\alpha)$ for which ω_i is maximum and integrate ω_i along the group velocity direction according to Gaster's transformation[3]. This "envelope method" is one of the approaches used in the COSAL code developed by Malik.[4]

In spatial theory, the introduction of an additional scalar in the dispersion relation makes the problem more difficult: the amplification rate vector $\vec{A}$ is no longer a scalar; it is a function of both α_i and β_i. As a result, a new relation is needed in the eigenvalue formulation.

In this paper we consider two completely different eigenvalue formulations and compare their predictions with measurements. The first formulation is based on the wave packet theory (saddle-point method) and the second is based on the assumption that the amplification vector $\vec{A}$ is normal to the wing leading edge. The experimental data correspond to measurements obtained at ONERA/CERT for a transonic swept wing. The tests have been conducted in a cryogenic wind tunnel at very low stagnation temperatures.

The following section describes the calculation method employing both eigenvalue formulations. Results are presented in the third section and the predictions of both methods are compared with measurements. The paper ends with a summary of the more important conclusions.

2.0 Description of the Computational Methods

The compressible stability equations and their boundary conditions are well known and are given in several references, see for example Ref. 4. With the parallel flow approximation, they can be written in the following dimensionless form:

Continuity:

$$i(\alpha u + \beta w - \omega)\hat{\rho} + \rho[\frac{d\hat{v}}{dy} + i(\alpha\hat{u} + \beta\hat{w})] + \frac{d\rho}{dy}\hat{v} = 0$$

$$(1)$$

*Visiting research student from München University, Germany
**Research engineer
†Visiting Research student from ENSAE, Toulouse, France
††Associate Professor
†††Professor and Chairman

x-Momentum

$$\rho[i(\alpha u + \beta w - \omega)(\alpha\hat{u} + \beta\hat{w}) + (\alpha\frac{du}{dy} + \beta\frac{dw}{dy})\hat{v}]$$

$$= -i(\alpha^2 + \beta^2)\frac{\hat{p}}{\gamma M_e^2} + \frac{\mu}{R}\{(\alpha\frac{d^2\hat{u}}{dy^2} + \beta\frac{d^2\hat{w}}{dy^2})$$

$$+ (\alpha^2 + \beta^2)[i\frac{d\hat{v}}{dy} - 2(\alpha\hat{u} + \beta\hat{w})]\}$$

$$+ \frac{2}{3}\frac{\lambda - \mu}{R}(\alpha^2 + \beta^2)[i\frac{d\hat{v}}{dy} - (\alpha\hat{u} + \beta\hat{w})]$$

$$+ \frac{1}{R}\frac{d\mu}{dT}(\alpha\frac{d^2u}{dy^2} + \beta\frac{d^2w}{dy^2})\hat{T}$$

$$+ \frac{1}{R}[(\frac{d\mu}{dT}\frac{d\hat{T}}{dy} + \frac{d^2\mu}{dT^2}\frac{dT}{dy}\hat{T})(\alpha\frac{du}{dy} + \beta\frac{dw}{dy})]$$

$$+ \frac{1}{R}\frac{d\mu}{dT}\frac{dT}{dy}[(\alpha\frac{d\hat{u}}{dy} + \beta\frac{d\hat{w}}{dy}) + i(\alpha^2 + \beta^2)\hat{v}] \qquad (2)$$

z-Momentum

$$\rho[i(\alpha u + \beta w - \omega)(\alpha\hat{w} - \beta\hat{u}) + (\alpha\frac{dw}{dy} - \beta\frac{du}{dy})\hat{v}]$$

$$= \frac{\mu}{R}[(\alpha\frac{d^2\hat{w}}{dy^2} - \beta\frac{d^2\hat{u}}{dy^2}) - (\alpha^2 + \beta^2)(\alpha\hat{w} - \beta\hat{u})]$$

$$+ \frac{1}{R}[\frac{d\mu}{dT}\frac{dT}{dy}(\alpha\frac{d\hat{w}}{dy} - \beta\frac{d\hat{u}}{dy}) + \frac{d\mu}{dT}(\alpha\frac{d^2w}{dy^2} - \beta\frac{d^2u}{dy^2})\hat{T}$$

$$+ (\frac{d\mu}{dT}\frac{d\hat{T}}{dy} + \frac{d^2\mu}{dT^2}\frac{dT}{dy}\hat{T})(\alpha\frac{dw}{dy} - \beta\frac{du}{dy})] \qquad (3)$$

y-Momentum

$$i\rho(\alpha u + \beta w - \omega)\hat{v} = -\frac{1}{\gamma M_e^2}\frac{d\hat{p}}{dy} + \frac{\mu}{R}[2\frac{d^2\hat{v}}{dy^2}$$

$$+ i(\alpha\frac{d\hat{u}}{dy} + \beta\frac{d\hat{w}}{dy}) - (\alpha^2 + \beta^2)\hat{v}]$$

$$+ \frac{2}{3}\frac{\lambda - \mu}{R}[\frac{d^2\hat{v}}{dy^2} + i(\alpha\frac{d\hat{u}}{dy} + \beta\frac{d\hat{w}}{dy})]$$

$$+ \frac{1}{R}\{i\frac{d\mu}{dT}(\alpha\frac{du}{dy} + \beta\frac{dw}{dy})\hat{T} + 2\frac{d\mu}{dT}\frac{dT}{dy}\frac{d\hat{v}}{dy}$$

$$+ \frac{2}{3}\frac{d}{dT}(\lambda - \mu)\frac{dT}{dy}[\frac{d\hat{v}}{dy} + i(\alpha\hat{u} + \beta\hat{w})]\} \qquad (4)$$

Energy

$$\rho[i(\alpha u + \beta w - \omega)\hat{T} + \frac{dT}{dy}\hat{v}] = -(\gamma - 1)[\frac{d\hat{v}}{dy}$$

$$+ i(\alpha\hat{u} + \beta\hat{w})] + \frac{\gamma\mu}{PrR}[\frac{d^2\hat{T}}{dy^2} - (\alpha^2 + \beta^2)\hat{T}$$

$$+ \frac{1}{k}[\frac{dk}{dT}\frac{d^2T}{dy^2} + \frac{d^2k}{dT^2}(\frac{dT}{dy})^2]\hat{T} + \frac{2}{k}\frac{dk}{dT}\frac{dT}{dy}\frac{d\hat{T}}{dy}\}$$

$$+ \gamma\frac{(\gamma - 1)}{R}M_e^2\{2i\mu(\alpha\frac{du}{dy} + \beta\frac{dw}{dy})\hat{v}$$

$$+ \frac{d\mu}{dT}(\frac{d^2u}{dy^2} + \frac{d^2w}{dy^2})\hat{T}$$

$$+ \frac{2\mu}{\alpha^2 + \beta^2}[(\alpha\frac{du}{dy} + \beta\frac{dw}{dy})(\alpha\frac{d\hat{u}}{dy} + \beta\frac{d\hat{w}}{dy})$$

$$+ (\alpha\frac{dw}{dy} - \beta\frac{du}{dy})(\alpha\frac{d\hat{w}}{dy} - \beta\frac{d\hat{u}}{dy})]\} \qquad (5)$$

$$y = 0, \qquad \hat{u} = \hat{v} = \hat{w} = \hat{T} = 0 \qquad (6a)$$

$$y \to \infty, \qquad \hat{u}, \hat{v}, \hat{w}, \hat{T} \to 0 \qquad (6b)$$

The above equations can be expressed as a first-order system by defining the following new variables with primes denoting differentiation with respect to y,

$$z_1 = \alpha\hat{u} + \beta\hat{w}, \quad z_2 = \alpha\hat{u}' + \beta\hat{w}', \quad z_3 = \hat{v}, \quad z_4 = \frac{\hat{p}}{\gamma M_e^2}$$

$$z_5 = \hat{T}, \quad z_6 = \hat{T}', \quad z_7 = \alpha\hat{w} - \beta\hat{u}, \quad z_8 = \alpha\hat{w}' - \beta\hat{u}'$$

$$(7)$$

In terms of these new variables, Eqs. (1) to (6), for a three-dimensional compressible flow can be written as

$$\underline{z}' = B\underline{z} \qquad (8)$$

where $\underline{z} = (z_1, z_2, \ldots, z_8)^T$ and B is a 8 x 8 coefficient matrix defined by

$$B = \begin{vmatrix} 0 & 1 & 0 & 0 & 0 & 0 & 0 & 0 \\ b_{21} & b_{22} & b_{23} & b_{24} & b_{25} & b_{26} & 0 & 0 \\ b_{31} & 0 & b_{33} & b_{34} & b_{35} & 0 & 0 & 0 \\ b_{41} & b_{42} & b_{43} & b_{44} & b_{45} & b_{46} & 0 & 0 \\ 0 & 0 & 0 & 0 & 0 & 1 & 0 & 0 \\ 0 & b_{62} & b_{63} & b_{64} & b_{65} & b_{66} & 0 & b_{68} \\ 0 & 0 & 0 & 0 & 0 & 0 & 0 & 1 \\ 0 & 0 & b_{83} & 0 & b_{85} & b_{86} & b_{87} & b_{88} \end{vmatrix} \qquad (9)$$

with its nonzero elements given in Appendix 1.

The solution of Eq. (8) subject to the boundary conditions given by

$$y = 0, \quad z_1 = z_3 = z_5 = z_7 = 0$$

$$y \to \infty, \quad z_1, z_3, z_5, z_7 \to 0 \tag{10}$$

can be obtained with two separate eigenvalue formulations as described in the following two subsections, 2.1 and 2.2.

2.1 Eigenvalue Formulation Based on the Direction of the Amplification Vector (ONERA/CERT Method)

The basic assumption of this method, first proposed by Mack,[7] is that on a wing with x and z denoting the coordinates normal to the leading edge and spanwise direction, amplification only occurs in the x-direction and not in the spanwise direction; that is,

$$\beta_i = 0 \tag{11}$$

This assumption, formulated for an infinite swept wing, reduces the number of unknown eigenvalues in the spatial theory from six to five. With ω and R given in the transition prediction problem, the unknown eigenvalues correspond to α_i, α_r and β_r. For an assumed β_r, the wave number α is then calculated so that the amplification rate α_i can be determined. Additional calculations are then performed for different values of β_r in order to determine the maximum amplification rate. This procedure, as in the saddle-point method, is repeated for each x-station and the n-factor in the e^n-method is calculated from

$$n = - \int_{x_0}^{x} (\alpha_i)_{max} dx \tag{12}$$

for different specified frequencies. Here x_0 corresponds to the x-station where the stability calculations are initiated. Transition is assumed to occur for the frequency for which the locally most unstable disturbance reaches a value of n between 8 and 10.

2.2 Eigenvalue Formulation Based on the Saddle-Point Method (CSC Method)

The Cebeci-Stewartson-Chen (CSC) method was first proposed and used by Cebeci and Stewartson

and is described in some detail in Ref. 7. In this method the relationship between the two wave numbers α and β is not assumed but computed from the requirement that $\partial\alpha/\partial\beta$ is real. According to this requirement, the wave orientation and growth direction of the disturbance are given by

$$\left(\frac{\partial\alpha}{\partial\beta}\right)_{\omega,R} = -\tan\gamma = -\frac{z}{x} \tag{13}$$

where γ denotes the angle that the disturbance makes with the x-axis, α and β are related by Eq. (13) and the disturbance propagating along the ray is given by the two terms on the right-hand side of Eq. (13). The disturbances are damped if the amplification rate Γ defined by

$$\Gamma = \alpha_i - \beta_i \left(\frac{\partial\alpha}{\partial\beta}\right)_{\omega,R} \tag{14}$$

is > 0, neutral if $\Gamma = 0$, and amplified if $\Gamma < 0$. Once α and β are computed with the constraints of Eq. (13), the amplification rate is obtained from Eq. (14); additional calculations are then made for different values of $\partial\alpha/\partial\beta$ so that new values of α and β are calculated to determine the maximum value of Γ. Further details of the solution procedure are given in Ref. 8.

3.0 Results and Discussion

3.1 Experimental Conditions

The experimental data used in our studies correspond to laminar flow on a 15-degree swept tapered wing. The chord is 0.228m at the root and 0.145m at the tip. The wing has a span of 0.39m with an AS409 cross-section and a trailing-edge sweep angle of three degrees. The height of the hollows on the wing is less than 0.05 mm (from peak to valley) for a chordwise extent of about 2 cm. In order to avoid the need to perform full three-dimensional stability/transition calculations, the measurements discussed in Ref. 9 and summarized in Ref. 10, were carried out under infinite swept conditions with the wing having a mean sweep angle of 12 degrees at an angle of attack of 0.3 degrees. The computations were made at a mean chord of 0.186m.

Figure 1 shows the Mach number distributions measured at different Reynolds numbers for a free-stream Mach number of 0.74 at two stagnation pressures. As can be seen, the Mach number distribution has "bumps" around x/c ≈ 0.3 and 0.47 caused
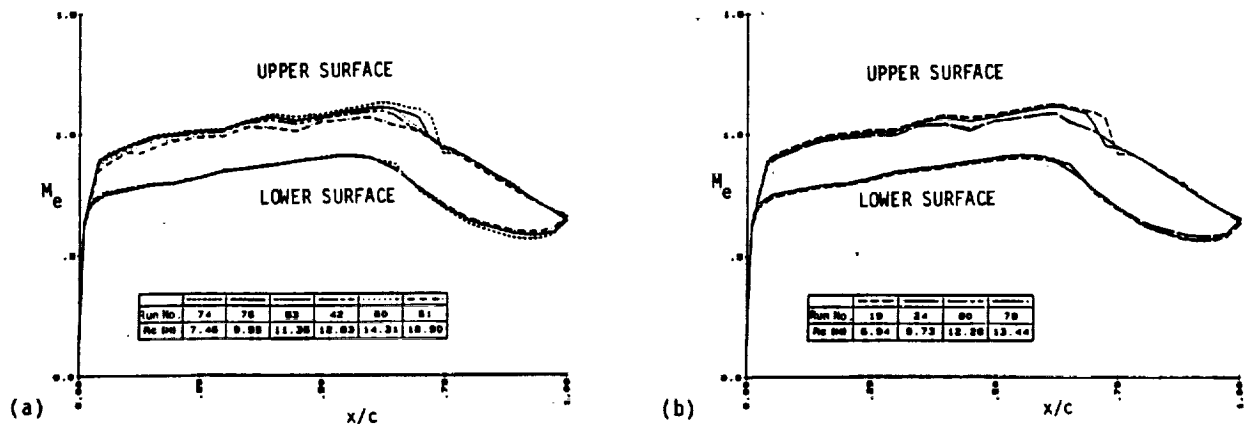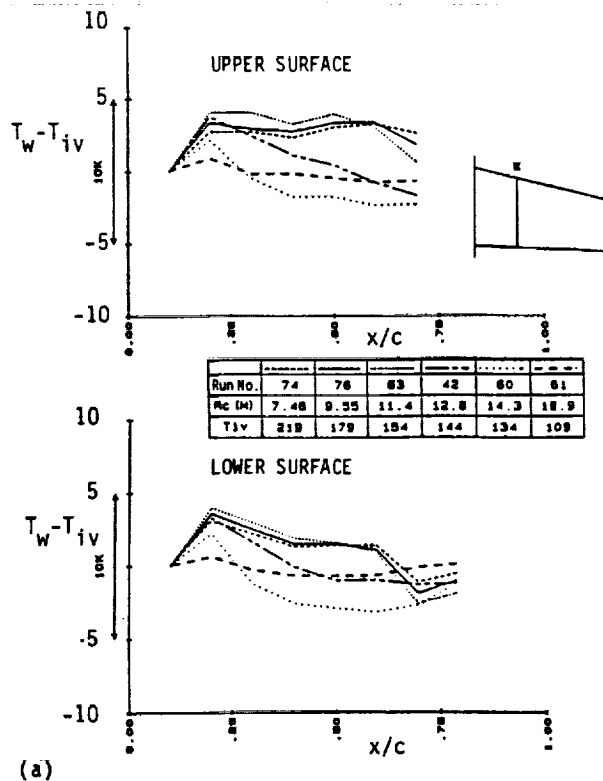
Fig. 1. Mach number distributions for $M_\infty = 0.74$, $\alpha = 0.3$, and $p_1 =$ (a) 2.0 bar, (b) 2.5 bar.

by small hollows in the model. On the lower surface, a smooth bend around x/c = 0.20 is visible. These discontinuities are common for all experiments and their effects on transition were part of the investigation conducted and discussed in detail in Ref. 10.

Figure 2 shows the variation of the experimental wall temperature distributions along the chord. Each distribution is referenced to its temperature, T_{1v}, measured at the first thermocouple in the flow direction. The maximum relative difference between the wall and freestream temperature is 5 degrees, which indicates that the influence of a nonadiabatic wall on transition must be considered. This includes the relative undulation as well as the absolute wall temperature.

Figure 3 shows the variation of the drag coefficient with Reynolds numbers at three stagnation pressures and several stagnation temperatures. Since the drag coefficient increases significantly for a turbulent boundary layer, it can be used as an indicator of transition. The evolution of C_d was measured in the cryogenic, transonic wind tunnel, T2, at ONERA/CERT for different stagnation pressures (1.7 to 2.5 bars) and different stagnation temperatures (between 165 and 109K). The values of C_d were obtained from wake measurements.

In the present study we consider two runs corresponding to 42 and 79, with Run 42 having a stagnation temperature of 145K and a stagnation pressure of 2.0 bar. The influence of higher temperature at a higher pressure is examined with run 79, which has a stagnation temperature of 165K and a stagnation pressure of 2.5 bar. In both cases we calculate only the upper surface of the wing.
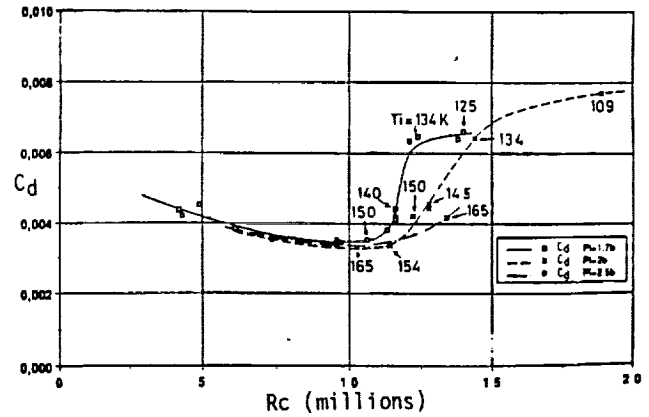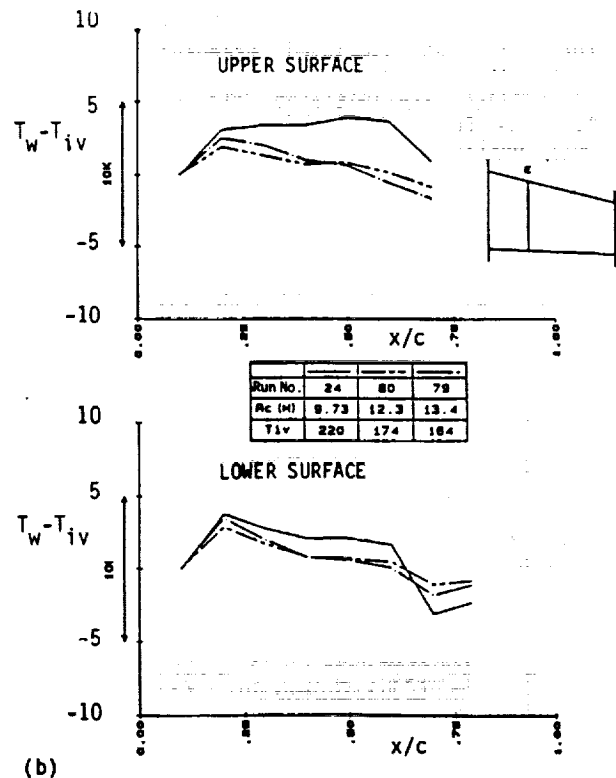

Fig. 3. Variation of the drag coefficient C_d with stagnation temperature T_1 and pressure p_1 as a function of Reynolds number R_c.
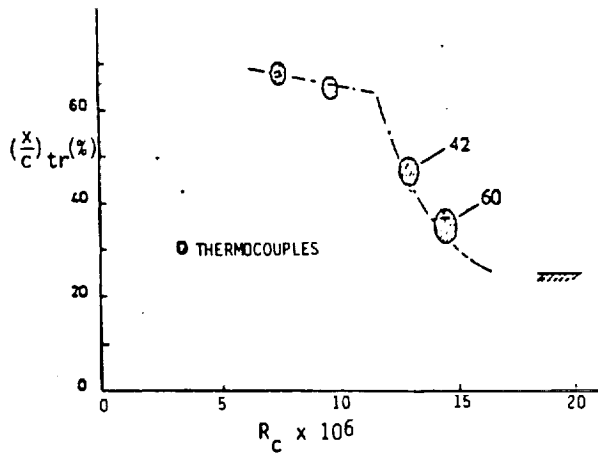
Additional studies are in progress for run 60, which has a stagnation temperature of 134K, and a stagnation pressure of 2.0 bar. These studies will be reported separately.

Figure 4 shows the experimental transition locations for runs 42 and 60. The location of transition was determined from the change of the wall temperature measured by thermocouples, along the chord, resulting from the different heat fluxes for laminar and turbulent flow. For run 79, the location of transition was assumed to be the same as that of run 42 because of the similar drag coefficient and Reynolds number (Fig. 3).
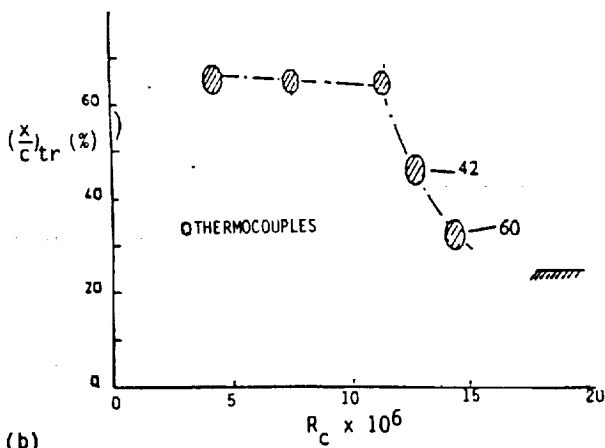

(a)

(b)

Fig. 2. Difference between the wall and freestream temperature, $M_\infty = 0.74$, $\alpha = 0.3$, $p_1 =$ (a) 2.0 bar, (b) 2.5 bar.
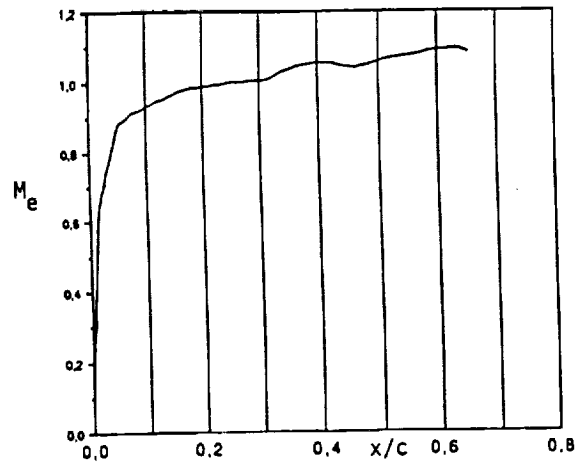
4

(a)

(b)

Fig. 4. Transition locations for runs 42 and 60, (a) upper surface, (b) lower surface.
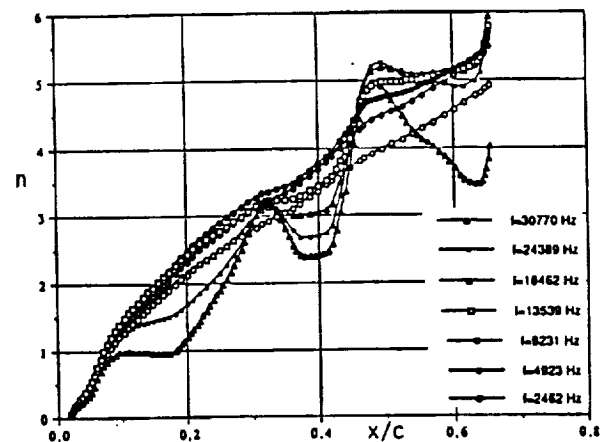
3.2 Calculations with the ONERA/CERT Method

A detailed discussion of the calculations for the experimental work described in the previous subsection is presented in Ref. 10. In this subsection we present results for runs 42 and 79 for Mach number distributions containing "bumps" around $x/c \approx 0.3$ and 0.47 caused by small hollows in the model and compare them with the calculations employing the CSULB method in subsection 3.3. Studies are in progress for Mach number distributions without bumps and will be reported separately.

The boundary-layer and stability calculations for run 42 were performed for an adiabatic wall and specified wall temperature distributions at a Reynolds number of 12.8×10^6. Figure 5 shows the predictions of the ONERA/CERT method for the adiabatic wall case together with the measured Mach number distribution (Fig. 5a) used in the boundary-layer calculations for a stagnation temperature of 145K and a stagnation pressure of 2.0 bar. According to Fig. 4, the location of transition corresponds to $x/c \approx 0.47$.
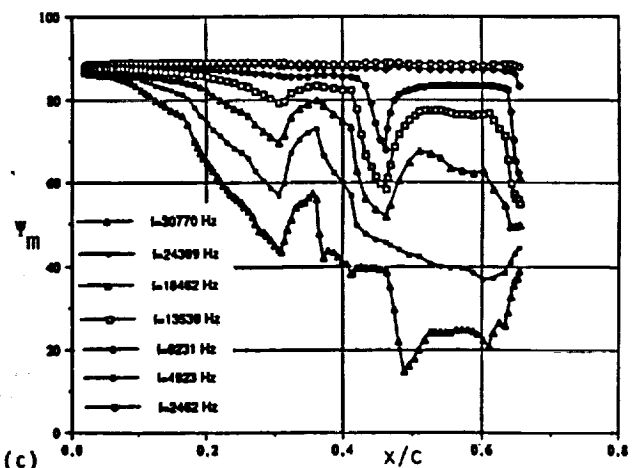
The calculated n-factors shown in Fig. 5b were obtained for seven frequencies which can be classified in three groups: (1) the high ones from

(a)

(b)

(c)

Fig. 5. Distributions of (a) Mach number, (b) computed n factors, and (c) the most unstable direction ψ_m of the disturbances for the adiabatic wall temperature distribution in Run 42 for the upper surface.

5

15 to 30 kHz, (2) the range from 9 to 15 kHz, and (3) the low ones from 2 to 9 kHz. Beginning with high frequencies, the calculations indicate rather strong undulations of n and of the wave directions ψ_m (Fig. 5c) along the chord. The undulations of n increase with frequency and show a strong dependence on the pressure gradient. Excluding the region of high rise of M_e (x/c ≈ 0 to 0.06, the following mechanism can be observed. A relative low pressure gradient has a stabilizing effect, whereas a higher, even positive pressure gradient is destabilizing. This effect becomes more and more distinct with increasing x/c. Looking, for example, at the n-curve with frequency 30770 Hz, we can see that the relative low pressure gradient between x/c ≈ 0.06 and 0.2 leads to an almost constant n. The increase of dp/dx between 0.2 and 0.3 leads to a strong rise of n. The steeper Mach number distribution from x/c ≈ 0.3 to 0.41 leads to a restabilization. The process is repeated as the pressure gradient changes again significantly at x/c ≈ 0.41 and 0.47.

Figure 6 shows the variation of the computed n values obtained for seven frequencies at the measured transition location of x/c ≈ 0.47. The maximum value of n is around 4.8 for a frequency of approximately 25 kHz. The computed value of n for transition is much lower than the value of n for this cryogenic wind tunnel T2 of CERT which has a freestream turbulence level of about 0.2% and a transition value of n between 7 and 8 based on experiments performed at ambient flow conditions.
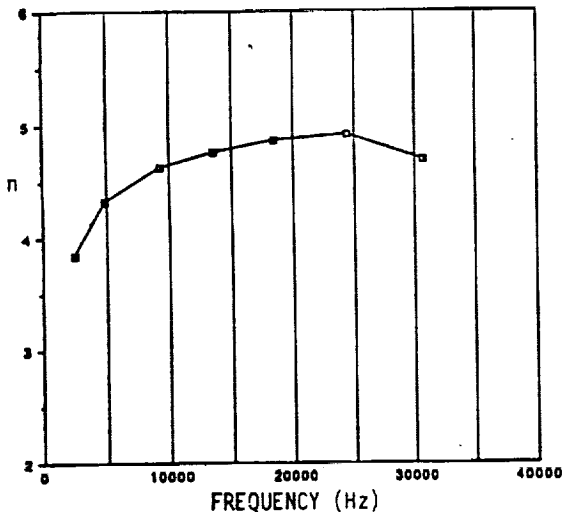

Fig. 6. Variation of n as a function of frequency at the transition point x/c ≈ 0.47.

To investigate the influence of wall temperature on the stability calculations, the following studies were conducted for specified wall temperature distributions. Figure 7 shows that the experimental wall temperature is higher than the adiabatic wall temperature and varies more along the chord. Since a higher wall temperature makes the boundary layer more unstable, it is plausible to assume that the stability calculations will yield higher values of n than those corresponding to adiabatic wall temperatures.

Figure 8 shows the computed results for the same two high and low frequencies studies previously. The characteristic shape of the curves has
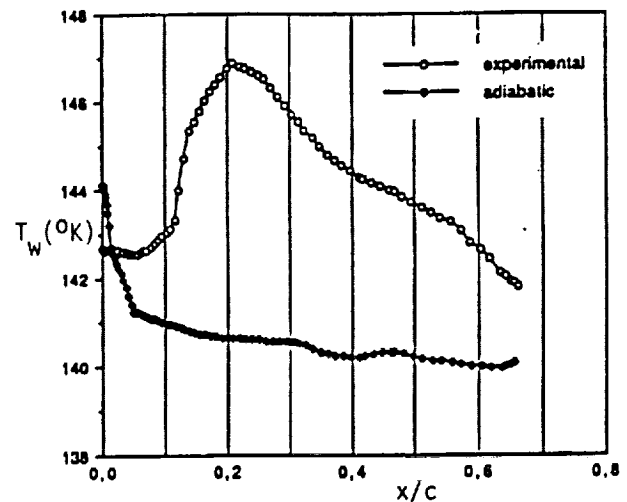

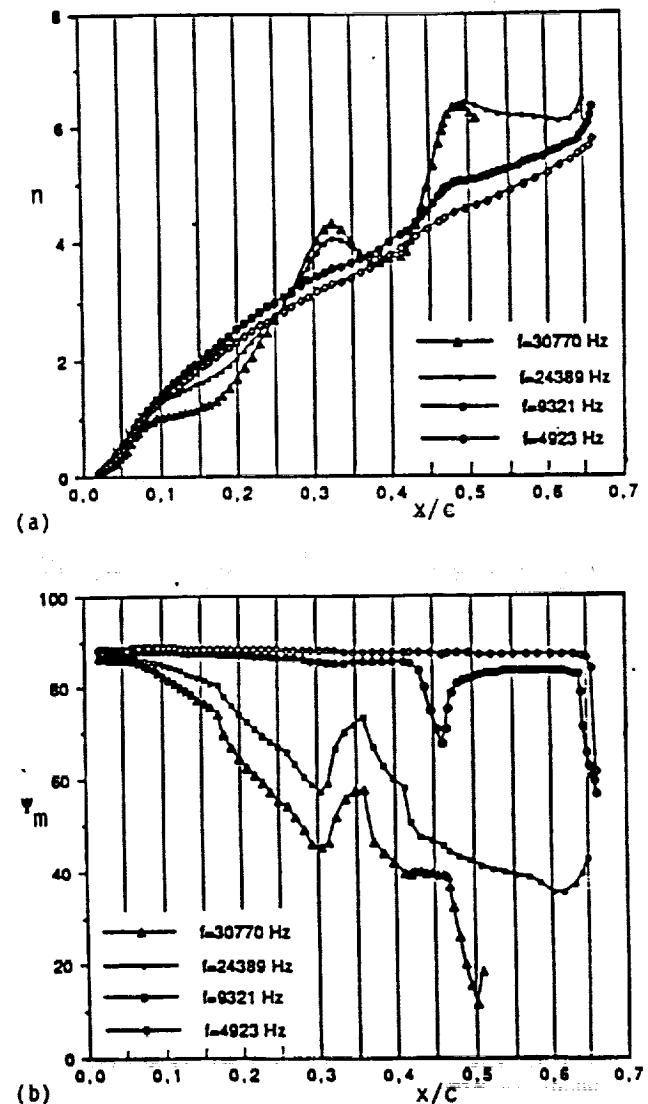Fig. 7. Comparison of measured and adiabatic wall temperature distributions along x/c.

(a)

(b)

Fig. 8. Distributions of (a) computed n factors and (b) the most unstable direction ψ_m of the disturbances for the experimental wall temperature distribution in run 42.
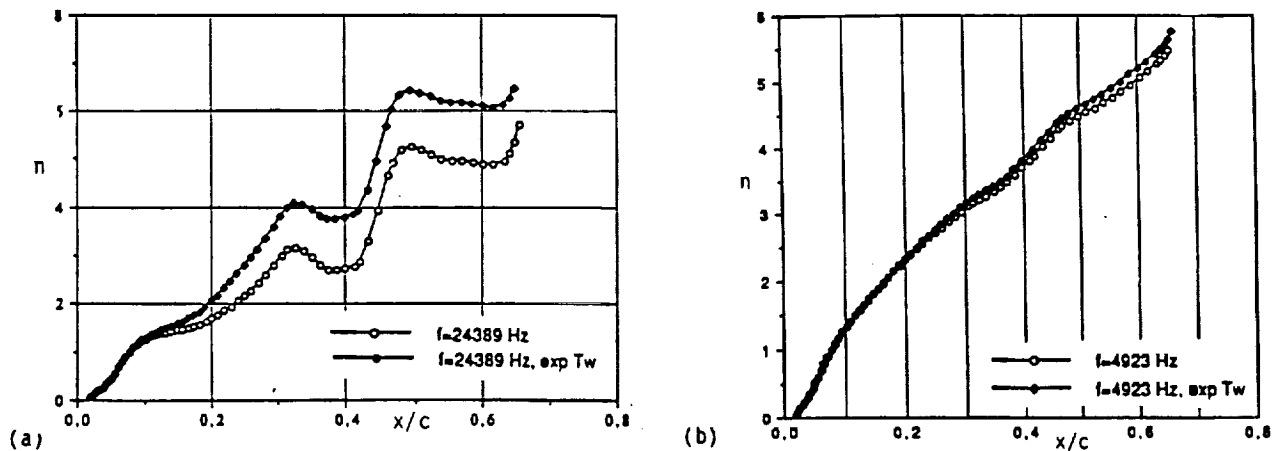
6

Fig. 9. Comparison of n-factor distributions for adiabatic and experimental wall temperature distributions in run 42, (a) high frequency case, (b) low frequency case.
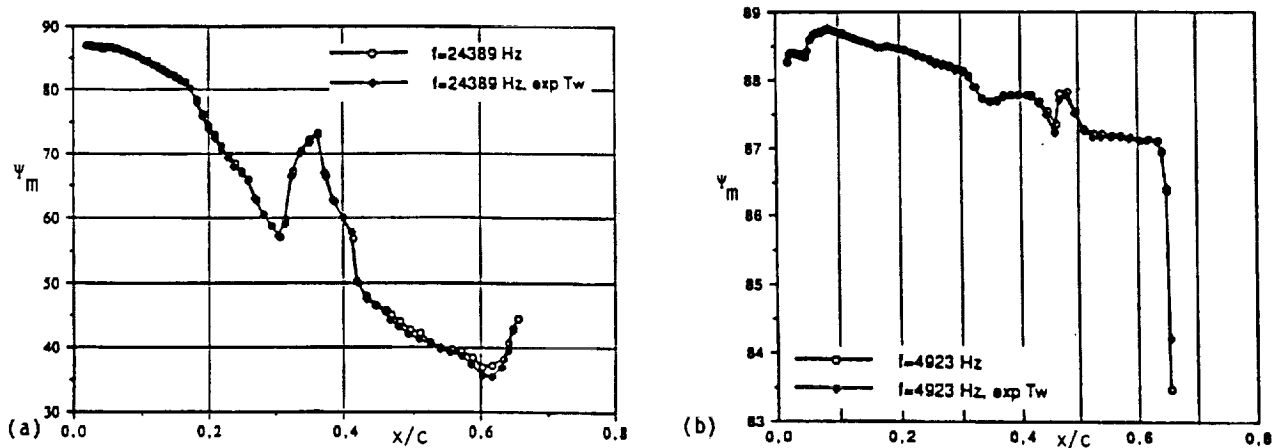

Fig. 10. Comparison of ψ_m distributions for adiabatic and experimental wall temperature distributions in run 42, (a) high frequency case, (b) low frequency case.

not changed and the previously discussed mechanisms for the adiabatic wall temperature calculations are still valid. However, in direct comparison with the adiabatic case, it can be observed that the results with high frequency (Fig. 9a) show a remarkably higher n distribution for x/c greater than 0.17 for the case of the experimental temperature distribution while the n curves for the lower frequencies are almost similar (see Fig. 9b). The ψ_m distributions for either case (see Fig. 10) show that the most unstable directions are independent of the wall temperature.

Figures 11 to 13 show the results for run 79 at a chord Reynolds number of 13.4×10^6. This case essentially has the same drag coefficient and Reynolds number as run 42. For this reason we assume the location of transition to be at x/c $\simeq$ 0.47.

Figure 11 shows the calculated n-factor distribution for an adiabatic wall temperature distribution and Fig. 12 shows the comparison of the n-factor distributions for adiabatic and experimental wall temperature distributions. As shown in Fig. 13, the temperature differences between adiabatic and measured wall temperatures for this run is weaker than for run 42. As a result, the distribution of n factors for both cases do not differ much from each other although, as in run
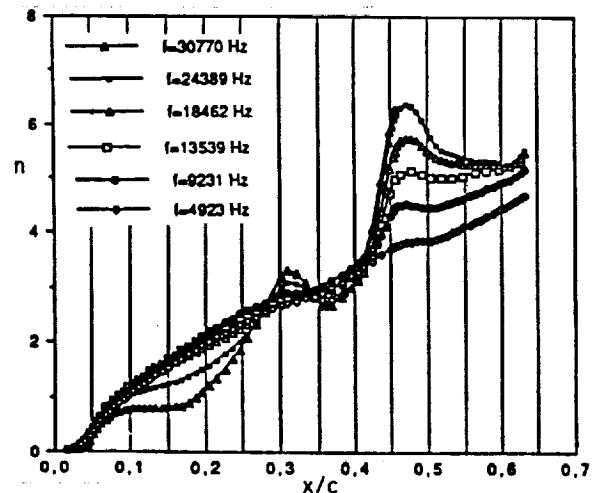

Fig. 11. Distribution of computed n factors for adiabatic wall conditions in run 79.

42, the measured wall temperatures lead to higher values of n than those obtained with adiabatic wall conditions. It can also be seen that, while the value of n at transition location, x/c = 0.47, is slightly over 7 for calculations performed with a measured wall temperature distribution, it is around 6.3 for adiabatic wall conditions.
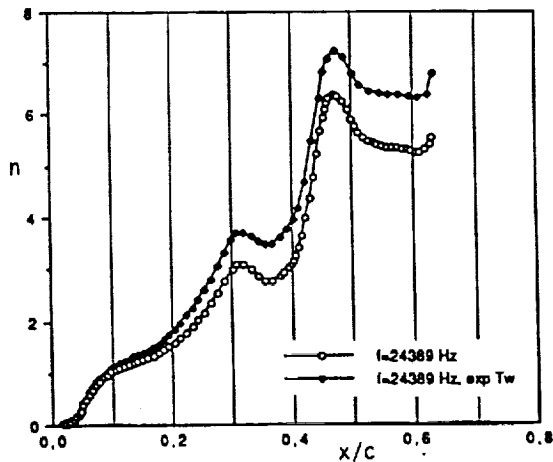
7

Fig. 12. Comparison of computed n factors for adiabatic and measured wall temperature distributions in run 79.

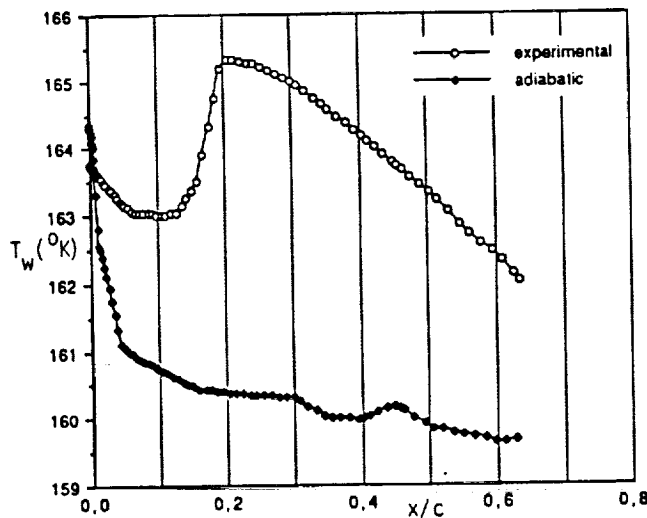
Fig. 13. Difference of real and adiabatic wall temperature distributions along x/c.

We note from the above results that near the leading edge (x/c < 0.10), all the unstable frequencies are of the crossflow type. Further downstream, the most unstable direction of the high frequencies decreases, leading to a more or less streamwise instability. It is interesting to note that this streamwise instability is very sensitive to small Mach number variations (hollows) as well as to the wall temperature. By contrast, the most unstable direction of the low frequencies remains close to 90°: they correspond to a crossflow instability which does not "see" the hollows (the evolution of the n-factor is monotonic). This instability is also not sensitive to the wall temperature variations. This is due to the fact that it is an "inflectional" instability governed by an inflection point located near the outer edge of the boundary layer.

3.3 Calculations with the CSC Method

A detailed description of the stability calculations for runs 42 and 79 are given in the previous section for the upper surface of the AS 409

wing. Similar detailed calculations have also been performed for the same runs, including run 60, using the CSC method described in subsection 2.2 and will be reported separately. In this subsection we shall present a summary of the predictions of the saddle-point method of Cebeci and Stewartson for the same runs, 42 and 79, by showing the distribution of n factors at several frequencies. We shall also present and discuss the procedure of determining the frequencies used in the calculation of amplification rates, which is different than any other method which employs a combination of linear stability theory and e^n-method to predict transition. In fact, the studies conducted with this method for incompressible flows on wings and bodies of revolution and recent studies in compressible flows over modern transport and military wings show that the calculation of the critical frequencies is the most important aspect of the transition prediction procedure using stability theory. The critical frequencies originate in a very narrow regions and require care and patience to compute their magnitudes and locations.

The frequencies needed in transition calculations are computed from zarfs recommended by Cebeci and Stewartson.[7] They essentially correspond to neutral stability curves in three-dimensional flows and have the following properties,
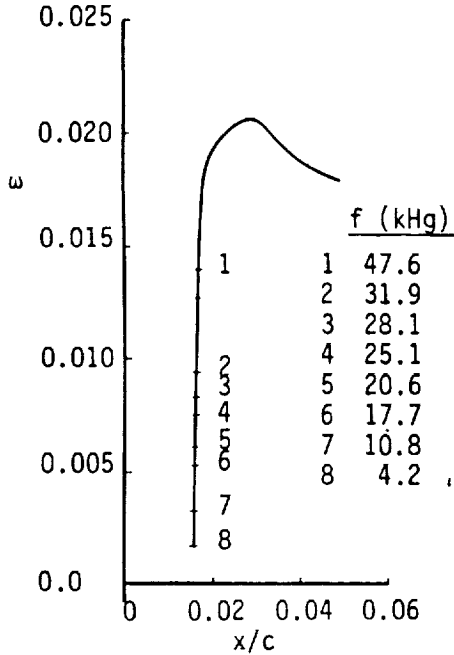
$$\alpha_i = \beta_i = 0, \qquad \frac{\partial \alpha}{\partial \beta} = real \qquad (15)$$

In the saddle-point method, for given velocity profiles obtained with the infinite-swept boundary-layer method of Cebeci, the stability calculations begin on the zarf where, with R known and α_i, β_i zero, the eigenvalue problem consists of calculating α_r, β_r and ω with the requirement given by Eq. (13). With the eigenvalues and disturbance angle γ of the zarf known at a specified x/c-location and with dimensional frequency specified, the calculations at the following x/c-station are performed to obtain α and β again with the requirement that $\partial \alpha/\partial \beta$ is real. This eigenvalue procedure is then repeated for different values of $\partial \alpha/\partial \beta$ or γ to find the value of γ for which Γ is maximum at each x/c-station. This process is repeated for each x/c-station, and n is calculated by evaluating the integral
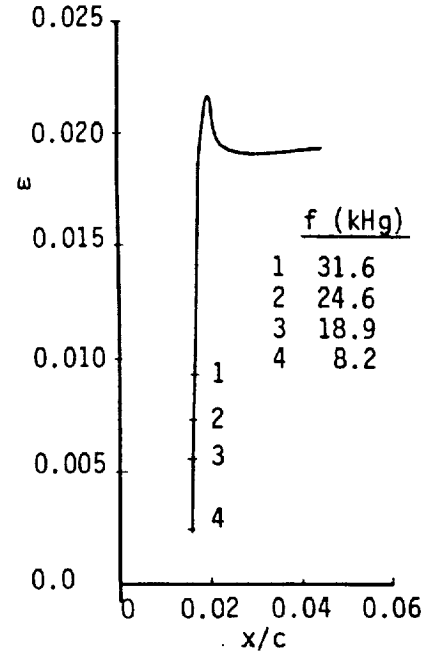
$$n = - \int_{x_0}^{x} \Gamma dx \qquad (16)$$

Figure 14 shows the zarfs for run 42 for an adiabatic wall and measured wall temperature distributions. As can be seen, the frequencies originate at nearly the same location (on a vertical line) and vary drastically one from another. Their calculation requires care and patience. A paper in preparation will discuss our procedure for generating them.

Figure 15 shows the computed n factors for the zarfs of Fig. 14. The results show that for adiabatic wall conditions, the maximum value of n for experimental transition location is around 6.3; the corresponding value for the measured wall temperature is 7.3. What is more important, however, is the fact that in the latter case, the computed transition location agrees very well with the observed location considering that the n-value for transition in this tunnel lies between 7 and 8.
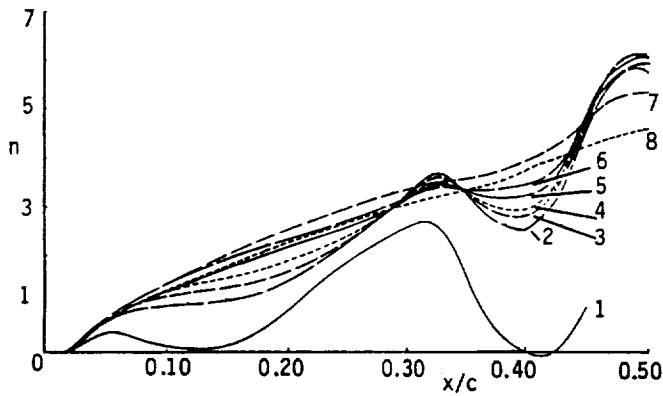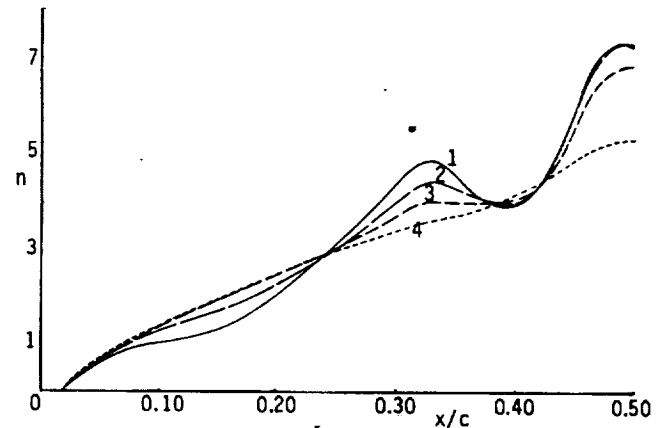
8

Fig. 14. Zarfs for run 42 for (a) adiabatic and (b) measured wall temperature distributions.

Fig. 15. Computed n-factors for run 42 for (a) adiabatic and (b) measured wall temperature distributions.

Figure 16 shows the zarfs for run 79 with wall conditions corresponding to adiabatic temperature and Fig. 17 shows a comparison between the zarfs obtained under adiabatic and measured wall temperature conditions. Again the steep rise in frequencies at almost one x/c-location is noted. The zarf calculations were performed for a very fine x/c-grid, since most of the frequencies start their amplification in an interval of 1/1000th of chord around 0.015. Figure 16 also shows zarfs away from the leading edge. These zarfs have low values of β_r around 10^{-2}, occur in an almost zero pressure gradient region and do not lead to amplification rates that grow significantly.

Figure 18 shows the computed n factors for run 79 with stability calculations performed for zarfs

in Fig. 17 under adiabatic and measured wall temperature conditions. For this flow, the n-value is much higher than those in run 42. For an adiabatic wall, it reaches a maximum value of around 8 and a value of around 9 for the measured wall temperature case. If we take the n value to be 7.5, a mid-n value of the expected n-value range for this wind tunnel, then transition occurs at x/c ≈ 0.46 for adiabatic wall conditions and x/c = 0.47 for measured wall temperature conditions. This compares well with inferred transition location of x/c = 0.47.

Figures 19 and 20 show a comparison between the calculated n-factors obtained with both methods, with results of CSC corresponding only to the disturbance that leads to transition. As can be
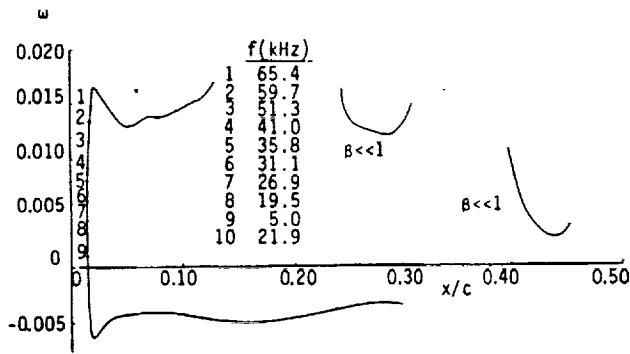
9

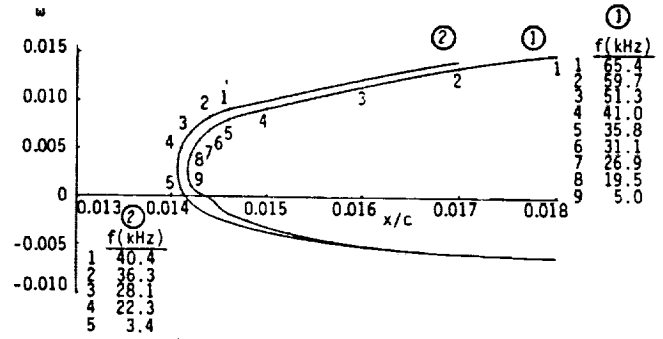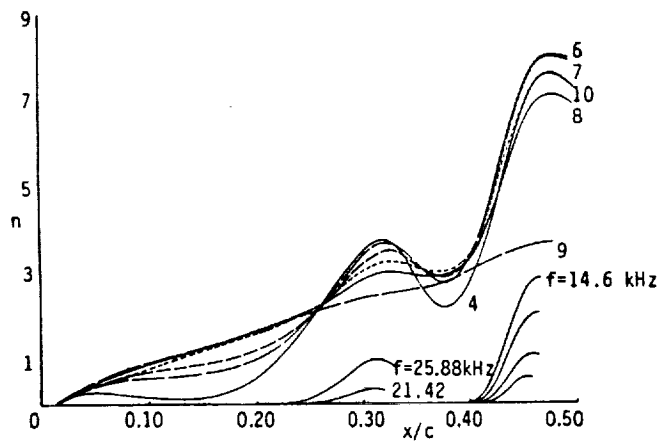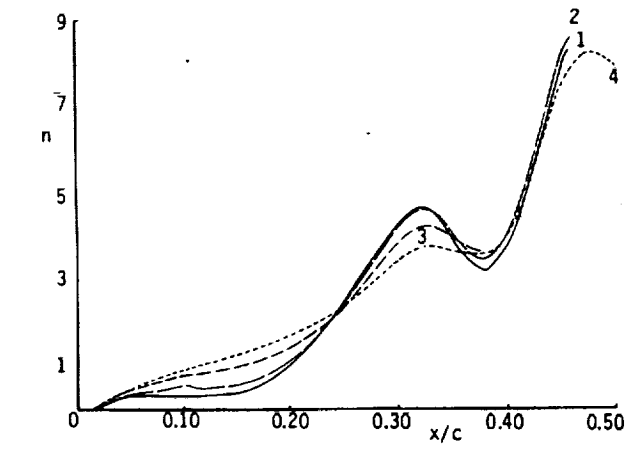Fig. 16. Zarfs for run 79 for adiabatic wall temperature distribution.

Fig. 17. Comparison between zarfs of run 79 for ① adiabatic and ② measured wall temperature distributions.
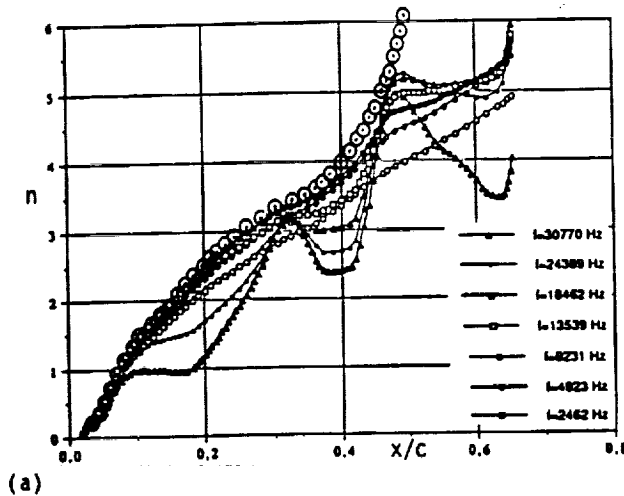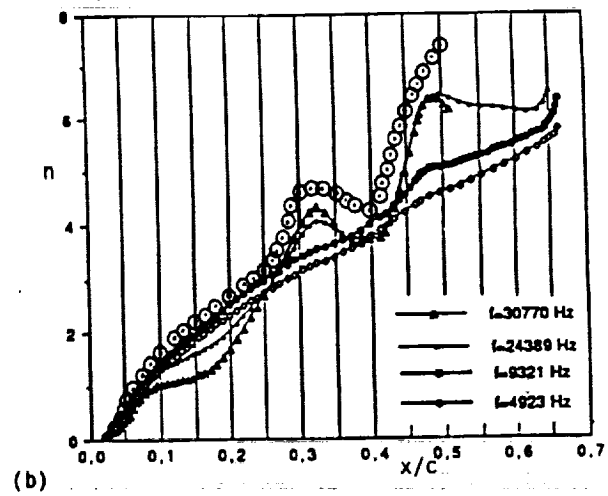

(a)

(b)

Fig. 18. Computed n-factors for run 79 for (a) adiabatic and (b) measured wall temperature distributions.
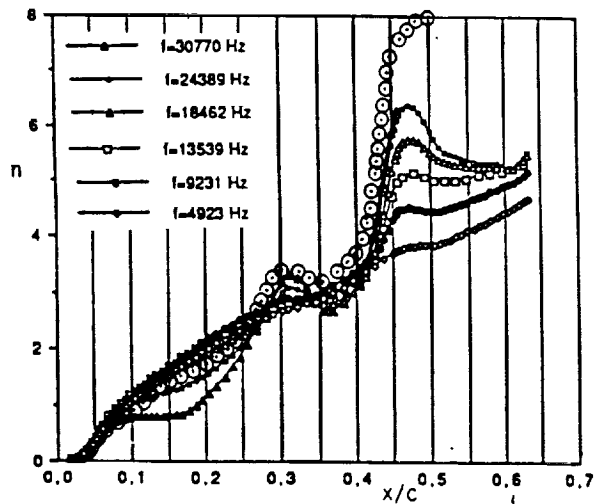

(a)

(b)

Fig. 19. Comparison between the predictions of CSC (denoted by circles ⊙) and ONERA/CERT methods for (a) adiabatic, and (b) measured wall temperature distributions in run 42.

seen, for x/c around 0.45, the calculations with the CSC method indicate higher values of the n-factor. The calculations with the ONERA/CERT method correlate the data with n between 6.5 and 7 while those of CSC with n between 7 and 8.

4.0 Concluding Remarks

Based on the studies reported here and in Refs. 9 and 10, the following two comments can be made. First, rather crude assumptions have been made in

10

(a)

(b)

Fig. 20. Comparisons between the predictions of CSC (denoted by circles ⊙) and ONERA/CERT methods for (a) abiabatic, and (b) measured wall temperature distributions in run 79.
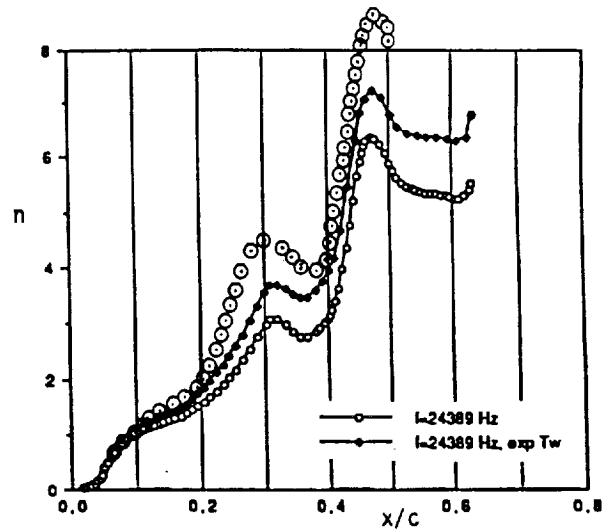
the computations (infinite swept wing assumption with a mean sweep angle and a mean chord). Second, it is possible that cryogenic conditions (temperature fluctuations) degrade the flow quality. This could explain the reason why the ONERA/CERT method calculates n-factors somewhat lower than those computed for ambient temperature with the same stability code. For stagnation temperatures lower than those considered in the paper, ice crystals appear on the model and trigger transition.

Acknowledgement: The authors are grateful to Dr. Y. Vigneron of Aerospatiale Toulouse (AS Toulouse) for giving them permission to publish the experimental data shown in Figures 1 to 4.

5.0 References

1. Smith, A.M.O. and Gamberoni, N., "Transition, Pressure Gradient, and Stability Theory," Proc. Int. Congress Appl. Mech., Vol. 9, Brussels, Vol. 4, p. 234, 1956.

2. Van Ingen, J.L., "A Suggested Semi-Empirical Method for the Calculation of the Boundary-Layer Region," Rept. No. VTH71, VTH74, Delft, Holland, 1956.

3. Gaster, M., "A Note on the Relation Between Temporally Increasing and Spatially Increasing Disturbances in Hydrodynamic Stability," J. Fluid Mech., Vol. 14, pp. 222-224, 1962.

4. Malik, M.R., "COSAL - A Black Box Compressible Stability Analysis Code for Transition Prediction in Three-Dimensional Boundary Layers," NASA CR 165 925, 1982.

5. Mack, L.M., "Boundary-Layer Stability Theory," AGARD Rept. No. 709, 1984.

6. Mack, L.M., "Stability of Three-Dimensional Boundary Layers on Swept Wings at Transonic Speeds," IUTAM Symposium, Transsonicum III, Göttingen, May 1988.

7. Cebeci, T. and Stewartson, K., "Stability and Transition in Three-Dimensional Flows," AIAA J., Vol. 18, pp. 398-405, 1980.

8. Cebeci, T., Chen, H.H., Arnal, D. and Huang, T.T., "A Three-Dimensional Linear Stability Approach to Transition on Wings and Bodies of Revolution at Incidence," to be published in AIAA J., December 1991.

9. Séraudie, A., Archambaud, J.P. and Payry, M.J., "Etude de la laminarité sur l'aile AS409 jusqu' a'des nombres de Reynolds de l'ordre de 14 millions dans la soufflerie T2," ONERA/CERT Internal Report No. 33/5006-19, June 1989.

10. Niethammer, R., "Boundary-Layer Stability Computations Related to Laminar Flow Experiments at Low Temperatures," Projet de fin D'etudes. Departement d'etudes et de recherches en aerothermodynamique, Toulouse Cedex, July 1991.

Appendix 1. Nonzero Elements of Matrix B.

$$\gamma_1 = \alpha u + \beta w - \omega, \quad \gamma_2 = \alpha^2 + \beta^2, \quad d = \frac{\lambda}{\mu}$$

$$\gamma_3 = \alpha \frac{du}{dy} + \beta \frac{dw}{dy}, \quad \gamma_4 = \alpha \frac{dw}{dy} - \beta \frac{du}{dy}$$

$$b_{21} = \frac{1R}{\mu T} \gamma_1 + \gamma_2, \quad b_{22} = -\frac{1}{\mu} \frac{d\mu}{dT} \frac{dT}{dy}$$

$$b_{23} = \frac{R\gamma_3}{\mu T} - \gamma_2 \frac{1}{\mu} \frac{d\mu}{dT} \frac{dT}{dy} - \frac{1+2d}{3} \gamma_2 \frac{1}{T} \frac{dT}{dy},$$

$$b_{24} = \frac{1R}{\mu} \gamma_2 - \frac{1+2d}{3} \gamma M_e^2 \gamma_2 \gamma_1$$

$$b_{25} = \frac{1+2d}{3T} \gamma_1 \gamma_2 - \frac{1}{\mu} \frac{d\mu}{dT} (\alpha \frac{d^2 u}{dy^2} + \beta \frac{d^2 w}{dy^2})$$

$$- \frac{1}{\mu} \frac{d^2 \mu}{dT^2} \frac{dT}{dy} \gamma_3$$

$$b_{26} = -\frac{1}{\mu}\frac{d\mu}{dT}\gamma_3, \quad b_{31} = -1, \quad b_{33} = \frac{1}{T}\frac{dT}{dy}$$

$$b_{34} = -1\gamma M_e^2\gamma_1,$$

$$b_{35} = \frac{1}{T}\gamma_1, \quad E = \frac{R}{\mu} + \frac{2}{3}1(2 + d)\gamma M_e^2\gamma_1$$

$$b_{41} = -\frac{1}{E}[-2b_{22} + \frac{2}{3}(2 + d)b_{33}], \quad b_{42} = -\frac{1}{E}$$

$$b_{43} = \frac{1}{E}[-\gamma_2 + \frac{2(2 + d)}{3\mu T}\frac{d\mu}{dT}(\frac{dT}{dy})^2$$

$$+ \frac{2(2 + d)}{3T}\frac{d^2T}{dy^2} - \frac{1R}{\mu T}\gamma_1]$$

$$b_{44} = -\frac{21}{3E}(2 + d)\gamma M_e^2(-\gamma_1 b_{22} + \gamma_3 + b_{22}\gamma_1)$$

$$b_{45} = \frac{1}{E}[\frac{1}{\mu}\frac{d\mu}{dT}\gamma_3 + \frac{2(2 + d)}{3T}(-b_{22}\gamma_1 + \gamma_3)]$$

$$b_{46} = \frac{21}{3ET}(2 + d)\gamma_1$$

$$b_{62} = -2(\gamma - 1)PrM_e^2(\frac{\gamma_3}{\gamma_2})$$

$$b_{63} = \frac{PrR}{\mu}b_{33} - 21(\gamma - 1)PrM_e^2\gamma_3$$

$$b_{64} = -\frac{1}{\mu}(\gamma - 1)PrRM_e^2\gamma_1$$

$$b_{65} = 1\frac{PrR}{\mu T}\gamma_1 + \gamma_2 - \frac{1}{k}\frac{dk}{dT}\frac{d^2T}{dy^2} - \frac{1}{k}\frac{d^2k}{dT^2}(\frac{dT}{dy})^2$$

$$- (\gamma - 1)PrM_e^2\frac{1}{\mu}\frac{d\mu}{dT}(\frac{d^2u}{dy^2} + \frac{d^2w}{dy^2})$$

$$b_{66} = -\frac{2}{k}\frac{dk}{dT}\frac{dT}{dy},$$

$$b_{68} = -\frac{2(\gamma - 1)}{\gamma_2}PrM_e^2\gamma_4$$

$$b_{83} = \frac{R}{\mu T}\gamma_4,$$

$$b_{85} = -\frac{1}{\mu}\frac{d\mu}{dT}(\alpha\frac{d^2w}{dy^2} - \beta\frac{d^2u}{dy^2}) - \frac{1}{\mu}\frac{d^2\mu}{dT^2}\frac{dT}{dy}\gamma_4$$

$$b_{86} = -\frac{1}{\mu}\frac{d\mu}{dT}\gamma_4, \quad b_{87} = \frac{1R}{\mu T}\gamma_1 + \gamma_2, \quad b_{88} = b_{22}$$